

# Maximally-localized Wannier orbitals and the extended Hubbard model for the twisted bilayer graphene

Mikito Koshino,<sup>1,\*</sup> Noah F. Q. Yuan,<sup>2</sup> Takashi Koretsune,<sup>3</sup> Masayuki Ochi,<sup>1</sup> Kazuhiko Kuroki,<sup>1</sup> and Liang Fu<sup>2</sup>

<sup>1</sup>*Department of Physics, Osaka University, Toyonaka 560-0043, Japan*

<sup>2</sup>*Department of Physics, Massachusetts Institute of Technology, Cambridge, Massachusetts 02139, USA*

<sup>3</sup>*Department of Physics, Tohoku University, Sendai 980-8578, Japan*

We develop an effective extended Hubbard model to describe the low-energy electronic properties of the twisted bilayer graphene. By using the Bloch states in the effective continuum model and with the aid of the maximally localized algorithm, we construct the Wannier orbitals and obtain an effective tight-binding model on the emergent honeycomb lattice. We found the Wannier state takes a peculiar three-peak form in which the amplitude maxima are located at the triangle corners surrounding the center. We estimate the direct Coulomb interaction and the exchange interaction between the Wannier states. At the filling of two electrons per super cell, in particular, we find an unexpected degeneracy of a charge-ordered state and a homogeneous state which would possibly lead to an unconventional many-body state.

## I. INTRODUCTION

The recent discovery of the superconductivity and strongly correlated insulating state in the twisted bilayer graphene (TBG)<sup>1,2</sup> attracts enormous attention and triggered a surge of theoretical works on this subject.<sup>3–16</sup> TBG is a bilayer system in which two graphene layers are rotationally stacked to each other,<sup>17–22</sup> where the electronic band structure sensitively depends on the twist angle  $\theta$ . In a small  $\theta$ , in particular, a slight difference in the lattice orientation gives rise to a long-period moiré interference pattern, causing a substantial modification of the Dirac dispersion.<sup>23–34</sup> Theoretically it was predicted that the Fermi velocity vanishes at certain  $\theta$ 's called the magic angles, around which nearly-flat bands with extremely narrow band width emerge at low energy.<sup>28,33</sup> The superconductivity was actually observed around a magic angle of  $1.05^\circ$ , where the insulating phase and the superconducting phase occur around the filling of two electrons per super cell.

It is a challenging problem to theoretically describe the many-body physics in TBG. At  $\theta = 1.05^\circ$ , the spatial period of the moiré pattern is more than 10 nm and the number of carbon atoms in a unit cell exceeds 10,000. The electronic property of such a huge and complex system can be calculated efficiently by the effective continuum model which captures the long-wavelength physics associated with the moiré period.<sup>23,28,29,31,34–36</sup> However, the effective continuum energy spectrum still contains a number of energy bands in the low-energy region, and we need one more step to simplify the model so as to exclusively describe the nearly-flat bands at lowest energy.

Actually the nearly-flat bands are separated by the energy gaps from other bands,<sup>1,37,38</sup> making it possible to construct an effective lattice model with well-localized Wannier orbitals purely consisting of the flat band states. Such an effective model was actually predicted by the symmetry analysis,<sup>4</sup> which concludes that the Wannier orbitals should be centered at non-equivalent AB point and BA point in the moiré pattern, to form an emergent

honeycomb lattice. Arguments and calculations suggesting a honeycomb lattice description have also been put forward in an independent work.<sup>5</sup> To obtain a concrete model with specific parameters, we need to construct the actual Wannier orbitals from the realistic model of TBG.

In this paper, we develop an extended Hubbard model of TBG at the magic-angle ( $\theta = 1.05^\circ$ ), based on the effective continuum model. By taking an appropriate linear combination of the Bloch states in the nearly flat bands, we build the Wannier orbitals centered at AB and BA points, and obtain the effective tight-binding model on the emergent honeycomb lattice. Here we adopted the maximally localized algorithm<sup>39</sup> to minimize the spread of the wave functions. From the obtained Wannier orbitals, we estimate the direct Coulomb energy and the exchange energy between electrons residing at different orbitals. The obtained Wannier state is centered at AB or BA point, while its maximum amplitude is found to be not at the center, but at three AA spots surrounding the center, as also noticed in Ref. 5. Importantly, we show explicitly that the pair of Wannier orbitals centered at a given AB or BA point has  $p_x, p_y$  on-site symmetry, hence forms a doublet under three-fold rotation around their centers, consistent with the symmetry analysis.<sup>4</sup>

Due to this peculiar three-peak form, the electron-electron interaction between the neighboring sites is as important as the on-site interaction term. At the filling of two electrons per super cell, in particular, we find an unexpected degeneracy of two different many-body states: a homogeneous state where an electron enters every sublattice of the effective honeycomb lattice, and a charge-ordered state where two electrons reside at every two sublattices [Fig. 7(a) and (b)]. We expect that such competing nature would possibly give rise to a nontrivial many-body ground state.

This paper is organized as follows: In Sec. II, we explain the atomic structure of TBG, and in Sec. III, we introduce the effective continuum model and argue the structure of the nearly-flat bands at the magic angle  $\theta = 1.05^\circ$ . In Sec. IV, we construct the Wannier orbitals

using the maximally localizing method, and obtain the tight-binding model in Sec. V. We consider the electron-electron interaction between the Wannier states in Sec. VI. A brief conclusion is presented in Sec. VII.

## II. ATOMIC STRUCTURE

We define the atomic structure of TBG by starting from AA-stacked bilayer graphene (i.e. perfectly overlapping honeycomb lattices) and rotating the layer 1 and 2 around a pair of registered  $B$ -sites by  $-\theta/2$  and  $+\theta/2$ , respectively. We define  $\mathbf{a}_1 = a(1, 0)$  and  $\mathbf{a}_2 = a(1/2, \sqrt{3}/2)$  as the lattice vectors of the initial AA-stacked bilayer before the rotation, where  $a \approx 0.246$  nm is the lattice constant of graphene. The corresponding reciprocal lattice vectors are  $\mathbf{a}_1^* = (2\pi/a)(1, -1/\sqrt{3})$  and  $\mathbf{a}_2^* = (2\pi/a)(0, 2/\sqrt{3})$ . After the rotation, the lattice vectors of layer  $l$  are given by  $\mathbf{a}_i^{(l)} = R(\mp\theta/2)\mathbf{a}_i$  with  $\mp$  for  $l = 1, 2$ , respectively, where  $R(\theta)$  represents the rotation by  $\theta$ . Likewise, the reciprocal lattice vectors become  $\mathbf{a}_i^{*(l)} = R(\mp\theta/2)\mathbf{a}_i^*$ . With respect to the registered  $B$ -sites, TBG has point group  $D_3$  generated by a three-fold in-plane rotation  $C_{3z}$  along  $z$ -axis and a two-fold rotation  $C_{2y}$  along  $y$ -axis.

In a small angle TBG, the slight mismatch of the lattice periods of two layers gives rise to a long-period moiré interference pattern. The reciprocal lattice vectors for the moiré pattern is given by  $\mathbf{G}_i^M = \mathbf{a}_i^{*(1)} - \mathbf{a}_i^{*(2)}$  ( $i = 1, 2$ ). The real-space lattice vectors  $\mathbf{L}_j^M$  can then be obtained from  $\mathbf{G}_i^M \cdot \mathbf{L}_j^M = 2\pi\delta_{ij}$ . A moiré unit cell is spanned by  $\mathbf{L}_1^M$  and  $\mathbf{L}_2^M$ . The lattice constant  $L_M = |\mathbf{L}_1^M| = |\mathbf{L}_2^M|$  is  $L_M = a/[2\sin(\theta/2)]$ . Figures 1(a) illustrates the atomic structure of TBG with  $\theta = 3.89^\circ$ . The lattice structure locally resembles the regular stacking such as AA, AB or BA depending on the position, where AA represents the perfect overlapping of hexagons, and AB (BA) is the shifted configuration in which  $A_1(B_1)$  sublattice is right above  $B_2(A_2)$ . In Fig. 1(a), AA points are located at the crossing points of the grid lines, and AB and BA points are at the centers of triangles indicated by dots. Figure 1(b) shows the corresponding folding of the Brillouin zone, where two large hexagons represent the first Brillouin zones of layer 1 and 2, and the small hexagon is the moiré Brillouin zone of TBG. The graphene's Dirac points (the band touching points) are located at  $\mathbf{K}_\xi^{(l)} = -\xi[2\mathbf{a}_1^{(l)*} + \mathbf{a}_2^{(l)*}]/3$  for layer  $l$ , where  $\xi = \pm 1$  is the valley index. We label the symmetric points of the reduced Brillouin zone as  $\bar{\Gamma}$ ,  $\bar{M}$ ,  $\bar{K}$  and  $\bar{K}'$  as in Fig. 1(b).

## III. EFFECTIVE CONTINUUM MODEL

When the moiré period is much longer than the atomic scale, the electronic structure can be described by an effective continuum model.<sup>23,28,29,31,34–36</sup> There the inter-

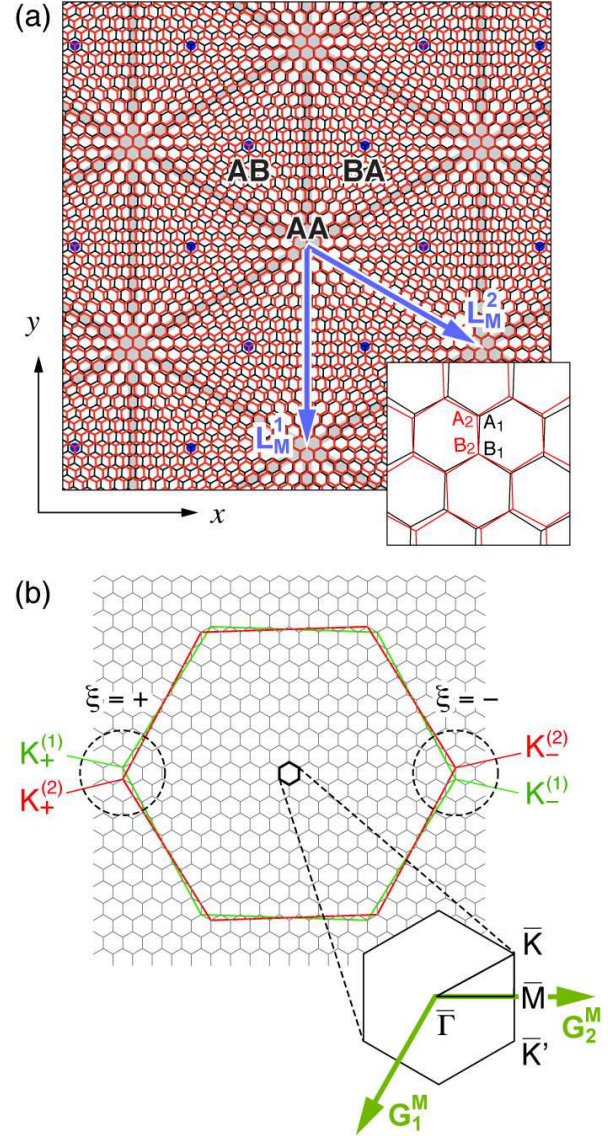


FIG. 1. (a) Atomic structure of TBG with  $\theta = 3.89^\circ$ . AA points are located at the crossing points of the grid lines, and AB and BA points are at the centers of triangles indicated by dots. (b) Brillouin zone folding in TBG with  $\theta = 3.89^\circ$ . Two large hexagons represent the first Brillouin zones of graphene layer 1 and 2, and the small hexagon is the moiré Brillouin zone of TBG.

valley mixing between  $\xi = \pm$  can be safely neglected and the total Hamiltonian is block-diagonalized into the two independent valleys. The effective Hamiltonian of continuum model for the valley  $\xi$  is written in a  $4 \times 4$  matrix for the basis of  $(A_1, B_1, A_2, B_2)$  as

$$H^{(\xi)} = \begin{pmatrix} H_1 & U^\dagger \\ U & H_2 \end{pmatrix}. \quad (1)$$

Here  $H_l$  ( $l = 1, 2$ ) is the intralayer Hamiltonian of layer  $l$ , which is given by the two-dimensional Weyl equation

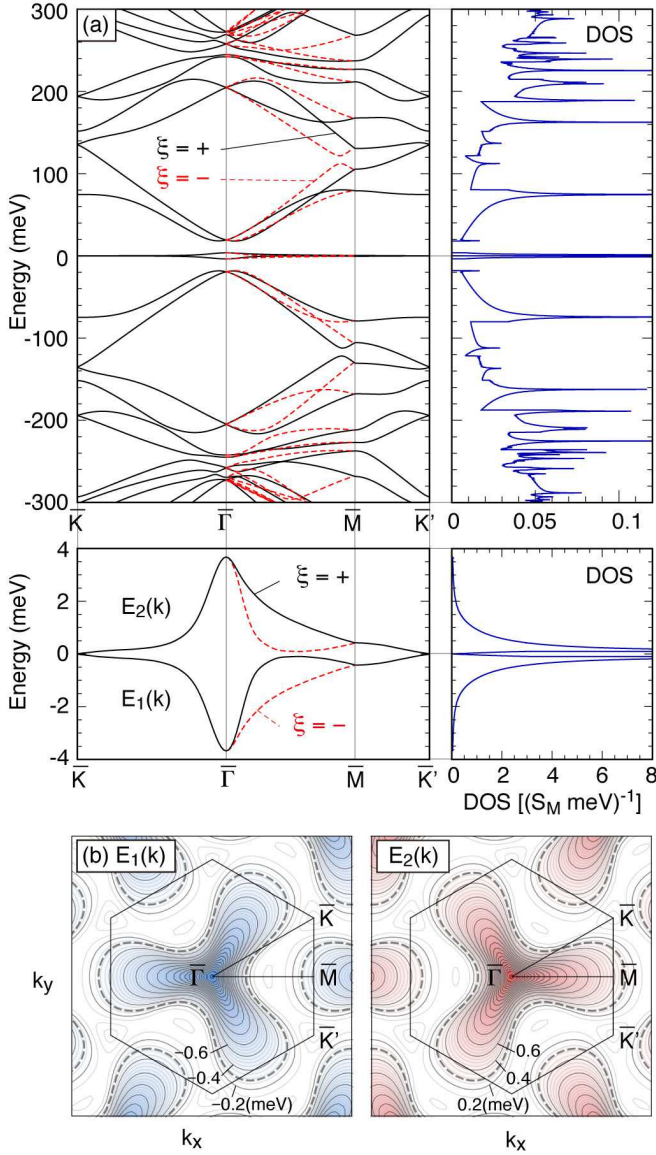


FIG. 2. (a) Energy band and the density of states of TBG at  $\theta = 1.05^\circ$ , where the lower panel is the enlarged plot of the zero-energy region. The black solid line and red dashed line represent the energy bands of  $\xi = \pm$  valleys, respectively. (b) Contour plots of  $E_1(\mathbf{k})$  and  $E_2(\mathbf{k})$  for the valley  $\xi = +$ . The dashed contour corresponds to the filling of two electrons / holes per super cell ( $n/n_0 = \pm 2$ ).

centered at  $\mathbf{K}_\xi^{(l)}$  point,

$$H_l = -\hbar v(\mathbf{k} - \mathbf{K}_\xi^{(l)}) \cdot (\xi \sigma_x, \sigma_y).$$

$U$  is the effective interlayer coupling given by<sup>34–36</sup>

$$U = \begin{pmatrix} U_{A_2 A_1} & U_{A_2 B_1} \\ U_{B_2 A_1} & U_{B_2 B_1} \end{pmatrix} = \begin{pmatrix} u & u' \\ u' & u \end{pmatrix} + \begin{pmatrix} u & u'\omega^{-\xi} \\ u'\omega^\xi & u \end{pmatrix} e^{i\xi \mathbf{G}_1^M \cdot \mathbf{r}} + \begin{pmatrix} u & u'\omega^\xi \\ u'\omega^{-\xi} & u \end{pmatrix} e^{i\xi (\mathbf{G}_1^M + \mathbf{G}_2^M) \cdot \mathbf{r}}, \quad (2)$$

where  $\omega = e^{2\pi i/3}$ . Here  $u$  and  $u'$  describe the amplitudes of diagonal and off-diagonal terms, respectively, in the sublattice space. The effective models in the previous studies<sup>34–36</sup> assume  $u = u'$ , which corresponds to a flat TBG in which the interlayer spacing  $d$  is constant everywhere. On the other hand, several theoretical studies predicted that the optimized lattice structure of TBG is actually corrugated in the out-of-plane direction, in such a way that  $d$  is the widest in AA stacking region and the narrowest AB / BA stacking region.<sup>40–43</sup> Here we incorporate the corrugation effect as a difference between  $u$  and  $u'$  in the effective model, of which detailed derivation is presented in the Appendix A. By using the parameters for the realistic system, we have  $u = 0.0797\text{eV}$  and  $u' = 0.0975\text{eV}$ . As we show in the following, the difference between  $u$  and  $u'$  introduces energy gaps between the lowest bands and the excited bands, in a qualitative agreement with the experimental observation.<sup>1,2,37</sup> It was found that the energy gaps isolating the lowest nearly-flat bands are also caused by the in-plane distortion.<sup>38</sup>

The calculation of the energy bands and the eigenstates is done in the  $k$ -space picture. For a single Bloch vector  $\mathbf{k}$  in the moiré Brillouin zone, the moiré interlayer coupling hybridizes the graphene's eigenstates at  $\mathbf{q} = \mathbf{k} + \mathbf{G}$ , where  $\mathbf{G} = m_1 \mathbf{G}_1^M + m_2 \mathbf{G}_2^M$  and  $m_1$  and  $m_2$  are integers. Therefore the eigenstate is written as a four-component wave function  $\psi_{n\mathbf{k}} = (\psi_{n\mathbf{k}}^{A_1}, \psi_{n\mathbf{k}}^{B_1}, \psi_{n\mathbf{k}}^{A_2}, \psi_{n\mathbf{k}}^{B_2})$  with

$$\psi_{n\mathbf{k}}^X(\mathbf{r}) = \sum_{\mathbf{G}} C_{n\mathbf{k}}^X(\mathbf{G}) e^{i(\mathbf{k} + \mathbf{G}) \cdot \mathbf{r}}, \quad (3)$$

where  $X = A_1, B_1, A_2, B_2$  is the sublattice index,  $n$  is the band index and  $\mathbf{k}$  is the Bloch wave vector in the moiré Brillouin zone. As the low-energy states are expected to be dominated by the individual graphenes' eigenstates near the original Dirac points, we pick up  $\mathbf{q}$ 's inside the cut-off circle  $|\mathbf{q} - \mathbf{q}_0| < q_c$ , where  $\mathbf{q}_0$  is taken as the midpoint between  $\mathbf{K}_\xi^{(1)}$  and  $\mathbf{K}_\xi^{(2)}$ , and  $q_c$  is set to  $4G_M$  ( $G_M = |\mathbf{G}_1^M| = |\mathbf{G}_2^M|$ ). Since the intervalley coupling can be neglected, the calculation is done independently for each of  $\xi = \pm$  as we discussed previously. We then numerically diagonalize the Hamiltonian within the limited wave space inside the cut-off circle and obtain the eigenenergies and eigenstates.

Figure 2(a) shows the energy band and the density of states of TBG at the magic angle  $\theta = 1.05^\circ$ , calculated by this approach. The lower panel is the enlarged plot of the zero-energy region where the near-flat bands are located. The black solid line and red dashed line represent



the energy bands of  $\xi = \pm$  valleys, respectively. They are the time-reversal partners to each other, and the energy bands of  $\xi = -$  are obtained just by inverting  $\mathbf{k}$  to  $-\mathbf{k}$ . The flat band cluster consists of two bands per spin and valley, which are denoted as  $E_1(\mathbf{k})$  and  $E_2(\mathbf{k})$  for the hole side and the electron side, respectively. The overall structure is about 7.5 meV wide in energy axis, and separated from the excited bands by the energy gap of about 14 meV in each of the electron side and the hole side. Figure 2(b) shows the contour plots of  $E_1(\mathbf{k})$  and  $E_2(\mathbf{k})$  for the valley  $\xi = +$ .  $E_1(\mathbf{k})$  and  $E_2(\mathbf{k})$  are trigonally warped in the opposite directions, so that  $E_1(\mathbf{k}) \neq E_1(-\mathbf{k})$  and  $E_2(\mathbf{k}) \neq E_2(-\mathbf{k})$ . The two bands are related by an additional particle-hole symmetry  $E_1(\mathbf{k}) = -E_2(-\mathbf{k})$ , while it is an artifact of the present model and not rigorous in the actual TBG.<sup>34</sup> The van-Hove singularity is located at  $E \approx \pm 0.13$  meV, which corresponds to the carrier density  $n/n_0 \approx \pm 0.68$  with spin and valley included, where  $n_0 = 1/S_M$ ,  $S_M = (\sqrt{3}/2)L_M^2$  is the moiré unit area (the band gap is  $n/n_0 = \pm 4$ ) and  $L_M$  is 13.4nm at  $\theta = 1.05^\circ$ . The filling of two electrons / holes per super cell ( $n/n_0 = \pm 2$ ) corresponds to  $E \approx \pm 0.28$  meV, which is indicated by dashed contours in Fig. 2(b).

#### IV. WANNIER ORBITALS

We construct the localized Wannier orbitals from the Bloch wave functions of the effective model. Since the nearly flat bands are energetically isolated from other bands, we expect that well-localized orbits can be made purely from the flat band states with all other bands neglected. The number of the independent Wannier orbitals in a unit cell coincides with the number of the energy bands taken into account, so we have two Wannier orbitals per spin and valley. According to the symmetry analysis<sup>4</sup>, the two orbitals should be centered at AB and BA points to form a honeycomb lattice. Our strategy is to first prepare certain initial orbitals centered at AB and BA, and then apply the maximally localized algorithm.<sup>39</sup> The following process is applied to  $\xi = \pm$  valleys separately, and we omit the valley index  $\xi$  hereafter.

The initial wave functions can be prepared as follows. First we fix the global phase factor of the Bloch states in two different ways: In gauge 1, we fix the phase so that  $\psi_{n\mathbf{k}}^{B_1}(\mathbf{r}_{BA})$  is real, and in gauge 2, we fix the phase so that  $\psi_{n\mathbf{k}}^{A_1}(\mathbf{r}_{AB})$  is real. Here  $\mathbf{r}_{BA} = (1/2, \sqrt{3}/2)(L_M/\sqrt{3})$  and  $\mathbf{r}_{AB} = (-1/2, \sqrt{3}/2)(L_M/\sqrt{3})$  are the positions of BA and AB points, respectively, measured from the AA point (0,0) [Fig. 1(a)]. We write the Bloch function in the gauge 1 as  $\psi_{n\mathbf{k}}$ , and that in the gauge 2 as  $e^{i\phi_{n\mathbf{k}}} \psi_{n\mathbf{k}}$ , where  $e^{i\phi_{n\mathbf{k}}}$  is the relative phase factor between gauge 1 and 2. We construct the initial Wannier orbitals 1 and 2 by summing the Bloch states of the bands  $\psi_{1\mathbf{k}}$  and  $\psi_{2\mathbf{k}}$

(corresponding to  $E_1(\mathbf{k})$  and  $E_2(\mathbf{k})$ , respectively) as,

$$\begin{aligned} |\mathbf{R}, 1\rangle_0 &= \frac{1}{\sqrt{N}} \sum_{\mathbf{k}} e^{-i\mathbf{k}\cdot\mathbf{R}} \frac{1}{\sqrt{2}} (|\psi_{1\mathbf{k}}\rangle + |\psi_{2\mathbf{k}}\rangle) \\ |\mathbf{R}, 2\rangle_0 &= \frac{1}{\sqrt{N}} \sum_{\mathbf{k}} e^{-i\mathbf{k}\cdot\mathbf{R}} \frac{1}{\sqrt{2}} e^{i\phi_{1\mathbf{k}}} (|\psi_{1\mathbf{k}}\rangle - |\psi_{2\mathbf{k}}\rangle), \end{aligned} \quad (4)$$

Here  $\mathbf{R} = n_1 \mathbf{L}_1^M + n_2 \mathbf{L}_2^M$  is the moiré lattice vector, and the summation in  $\mathbf{k}$  is taken over  $N$  discrete points in the moiré Brillouin zone. We take  $N = 18 \times 18$  in this study. It is straightforward to check the orthonormality,  $\langle \mathbf{R}', n' | \mathbf{R}, n \rangle_0 = \delta_{\mathbf{R}, \mathbf{R}'} \delta_{n, n'}$ .

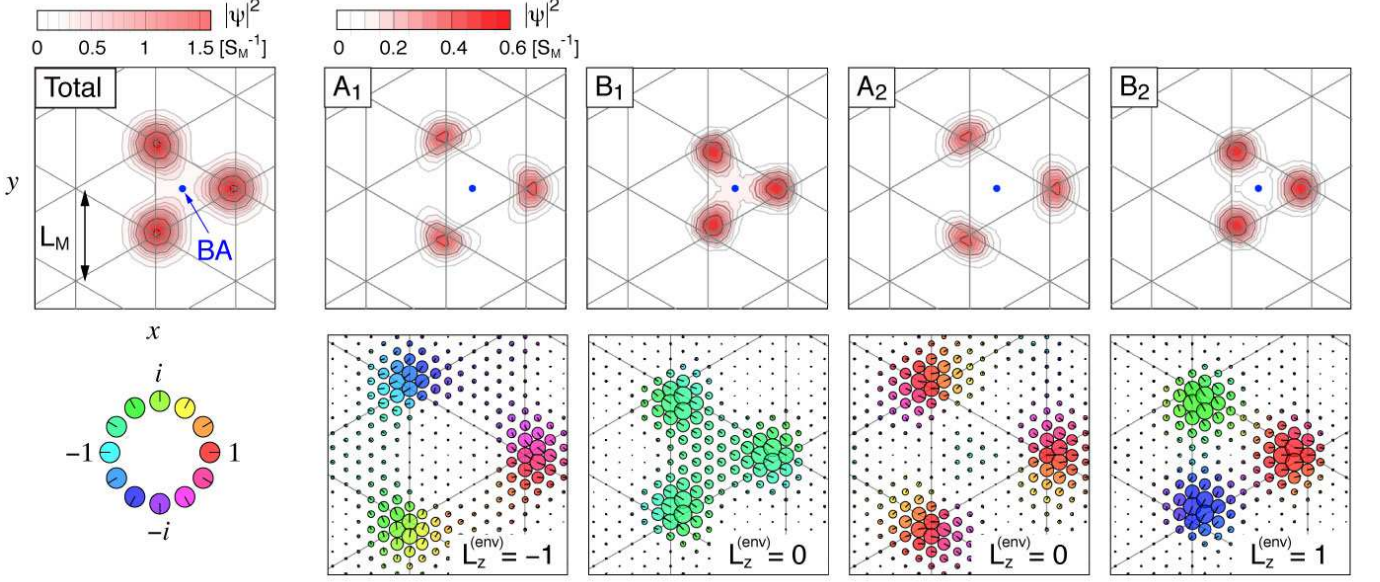
While  $|\mathbf{R}, 1\rangle_0$  and  $|\mathbf{R}, 2\rangle_0$  are already well localized around the center positions  $\mathbf{R} + \mathbf{r}_{BA}$  and  $\mathbf{R} + \mathbf{r}_{AB}$ , respectively, we can even reduce the spread of the wave function by maximally localizing method<sup>39</sup>. The final expression for the orbital  $n (= 1, 2)$  is given by

$$|\mathbf{R}, n\rangle = \frac{1}{\sqrt{N}} \sum_{\mathbf{k}} e^{-i\mathbf{k}\cdot\mathbf{R}} \sum_{m=1,2} U_{mn}^{(\mathbf{k})} |\psi_{m\mathbf{k}}\rangle, \quad (5)$$

where  $U_{mn}^{(\mathbf{k})}$  is a  $2 \times 2$  unitary matrix. The algorithm optimizes  $U_{mn}^{(\mathbf{k})}$  to minimize the spread functional. We put Eq. (4) as the initial value of  $U_{mn}^{(\mathbf{k})}$ , and iterate the minimization process until the convergence. In each step, we impose the symmetry constraint to  $U_{mn}^{(\mathbf{k})}$ . The optimized Wannier orbitals for the valley  $\xi = +$  are illustrated in Fig. 3. Those for the opposite valley  $\xi = -$  are given by the complex conjugate. For each of orbital 1 and 2, the top five panels show the contour maps for the squared amplitudes of the total wave function and of the four sublattice components. We actually see that the orbital 1 and 2 are centered at BA and AB positions, respectively, while the maximum of the wave amplitudes are located not at the center, but near three AA points surrounding the center. This reflects the fact that the Bloch wave functions of the nearly-flat bands are mostly localized AA spot of the moiré pattern.<sup>25,40</sup>

The lower panels illustrate the phase of the envelope function  $F^{X_l}(\mathbf{r})$  ( $X = A, B$  and  $l = 1, 2$ ) on some sample points, where the total wave function is  $\psi^{X_l}(\mathbf{r}) = e^{i\mathbf{K}_\xi^{(l)} \cdot \mathbf{r}} F^{X_l}(\mathbf{r})$ . Here the absolute value of  $F^{X_l}(\mathbf{r})$  is indicated by the radius of a circle, and its phase factor is by the direction of a bar and also by color. Now we see that the envelope functions on different sublattices have different eigenvalues of  $C'_{3z}$ , in-plane rotation with respect to its own center. However, noting that the Bloch factor  $e^{i\mathbf{K}_\xi \cdot \mathbf{r}}$  also carries a non-zero eigenvalue of  $C'_{3z}$ , the total wave function  $\psi = (\psi^{A_1}, \psi^{B_1}, \psi^{A_2}, \psi^{B_2})$  is found to be an eigenstate of  $C'_{3z}$  with a single eigenvalue. In orbital 1, for example, the  $C'_{3z}$  eigenvalue of  $F^{X_l}$  is  $(\omega, 1, 1, \omega^*)$  for  $(A_1, B_1, A_2, B_2)$ , so that the angular momentum of the envelope function is written as  $L_z^{(\text{env})} = (-1, 0, 0, 1)$ . On the other hand, the  $C'_{3z}$  eigenvalue for the Bloch factor  $e^{i\mathbf{K}_\xi \cdot \mathbf{r}}$  can be found by noting that BA point (the orbital center) coincides with  $A_1$  site and the center of hexagon of layer 2 [Fig. 1(a)], and then

## Orbital 1



## Orbital 2

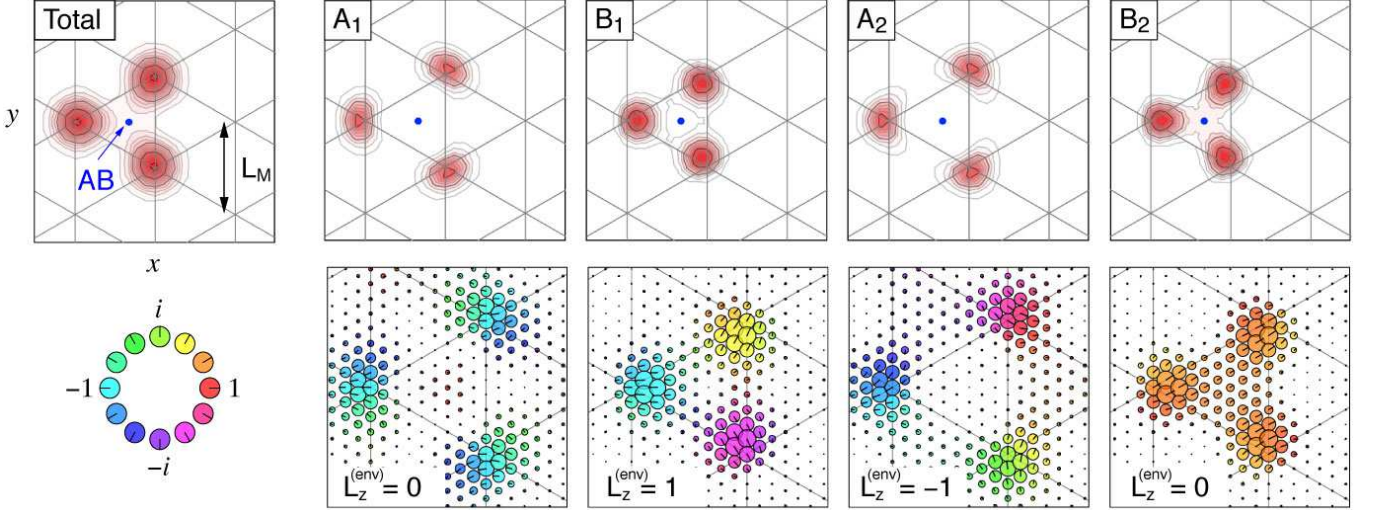


FIG. 3. Maximally localized Wannier orbitals of the valley  $\xi = +$ , in the low-energy flat band of TBG with  $\theta = 1.05^\circ$ . For each of orbital 1 and 2, the top five panels show the contour maps for the squared amplitudes of the total wave function and of the four sublattice components. The lower panels illustrate the phase of the envelope function on some sample points, where the amplitude is indicated by the radius of a circle, and its phase factor is by the direction of a bar and also by color.

we obtain  $L_z^{(\text{Bloch})} = (0, -1, -1, 1)$ . Therefore, the total angular momentum  $L_z = L_z^{(\text{env})} + L_z^{(\text{Bloch})}$  is  $-1$  for all the sublattices. Similarly, we can show  $L_z = -1$  also for orbital 2. Since the Wannier functions at the opposite valleys are related by the complex conjugate, we finally conclude that the eigenvalue of  $C'_{3z}$  is  $\omega^\xi = e^{\xi 2\pi i/3}$  for both orbital 1 and 2. Namely orbital 1 and 2 from the same valley  $\xi$  have the same nonzero angular momentum  $L_z = -\xi$ , in accordance with the symmetry analysis.<sup>4</sup> Due to the nonzero angular momentum, it is consistent that at its center (AB or BA points) the Wannier orbital

vanishes and the amplitude peaks are away from the center. We will discuss more on the symmetry properties of Wannier orbitals later in the next section.

## V. EFFECTIVE TIGHT-BINDING MODEL

From the Wannier orbitals and the energy bands, we can derive the effective tight-binding model to exactly reproduce the dispersion of the nearly-flat bands. In a straightforward calculation, the hopping integral between

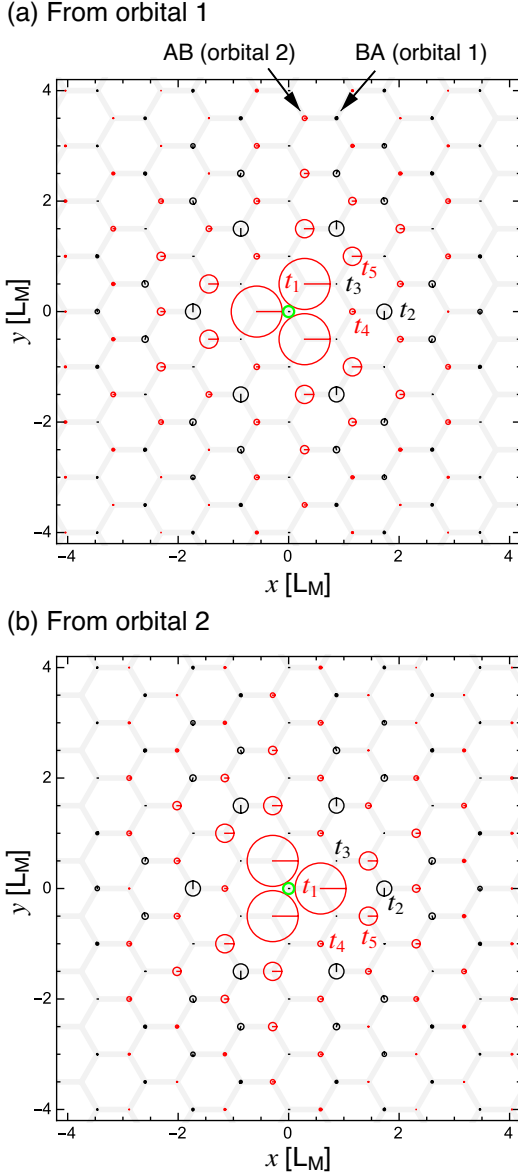


FIG. 4. Hopping integrals in the effective tight-binding model for the low-energy flat band of TBG at  $\theta = 1.05^\circ$ . The panel (a) and (b) present the hopping parameters from the Wannier orbital 1 and 2, respectively, where the radius of the circle at each lattice point indicates the absolute value of the hopping integral from the origin to that point, and the direction of the bar represents the phase in the complex plane.

the Wannier orbitals is written as

$$\begin{aligned} & \langle \mathbf{R}', n' | H | \mathbf{R}, n \rangle \\ &= \frac{1}{N} \sum_{\mathbf{k}} e^{i\mathbf{k} \cdot (\mathbf{R}' - \mathbf{R})} \left[ \hat{U}(\mathbf{k})^\dagger \begin{pmatrix} E_1(\mathbf{k}) & 0 \\ 0 & E_2(\mathbf{k}) \end{pmatrix} \hat{U}(\mathbf{k}) \right]_{n'n}, \end{aligned} \quad (6)$$

where  $\hat{U}(\mathbf{k})$  represents the matrix  $U_{mn}^{(\mathbf{k})}$ , and we used  $\langle \psi_{n'\mathbf{k}'} | H | \psi_{n\mathbf{k}} \rangle = \delta_{nn'} \delta_{\mathbf{k}\mathbf{k}'} E_n(\mathbf{k})$ . In Fig. 4(a) and (b), we

plot the hopping integrals from orbital 1 and 2, respectively, for the valley  $\xi = +$ . Here the honeycomb lattice represents the network of BA spots (orbital 1) and AB spots (orbital 2). The radius of the circle at each lattice point indicates the absolute value of the hopping integral from the origin (green circle at the center) to that point, and the direction of the bar represents the phase in the complex plane. The effective tight-binding model for the valley  $\xi = -$  is just given by taking the complex conjugate. The list of the hopping integrals for the valley  $\xi = +$  is included in Supplementary Material.<sup>44</sup>

To understand this effective tight-binding model, we need to analyze the symmetry properties of Wannier orbitals under point group  $D_3$ , as in Ref. 4. Recall that orbitals 1 and 2 have nonzero angular momentum  $L_z = -\xi$  at the valley  $\xi$ . Furthermore, under two-fold rotation  $C_{2y}$  which interchanges two graphene layers, we find orbital 1 from valley  $\xi$  is mapped to orbital 2 from valley  $-\xi$  and vice versa as shown in Fig. 3. Hence we can regard orbitals 1 and 2 from valley  $\xi$  as the  $p$ -wave-like orbitals  $p_\xi \equiv p_x + i\xi p_y$  residing on BA and AB points respectively. The angular momentum of  $p_\xi$  orbital is  $L_z = -\xi$  whether its center is at BA or AB point, which is consistent with  $L_z$  of orbital 1 and 2. Under  $C_{2y}$  the two graphene layers and hence BA and AB points are interchanged, and  $(p_x, p_y) \rightarrow (-p_x, p_y)$  or  $p_\xi \rightarrow -p_{-\xi}$ . In other words,  $C_{2y}$  interchanges  $p_\xi$  orbital at BA point and  $p_{-\xi}$  orbital at AB point, which reproduces the symmetry transformation of orbital 1 and 2 under  $C_{2y}$ .

Once we identify the symmetries of orbital 1 and 2, the tight-binding model then describes hopping among  $(p_x, p_y)$  orbitals on the honeycomb lattice formed by BA and AB spots, which reads

$$H = \sum_{\xi=\pm} \sum_{ij} t(\mathbf{r}_{ij}) e^{i\xi\phi(\mathbf{r}_{ij})} c_{i\xi}^\dagger c_{j\xi} + h.c., \quad (7)$$

where  $c_{i\xi}$  annihilates a  $p_\xi$ -orbital electron at site  $i$ ,  $\mathbf{r}_{ij}$  is the vector from site  $i$  to  $j$ , and  $t(\mathbf{r})$ ,  $\phi(\mathbf{r})$  are as shown in Fig. 4 (a) and (b).

The tight-binding model of Eq. (7) has U(1) symmetry in orbital space and SU(2) symmetry in spin space. As discussed in Ref. 4, the microscopic reason for U(1) symmetry is that at small twist angles the intervalley coupling is strongly suppressed and hence U(1) symmetry is not protected by crystal symmetries of  $D_3$ . Besides U(1) symmetry, Eq. (7) also has two properties not protected by point group  $D_3$ : The particle-hole symmetry  $E_1(\mathbf{k}) = -E_2(-\mathbf{k})$ , and the existence of the Dirac nodes at  $\bar{K}$ ,  $\bar{K}'$  points. These properties affect the hopping integrals and fix the magnitude and phase of special hopping terms. To be specific, we consider the nearest five hopping integrals  $t_1$  to  $t_5$  shown in Fig. 4 (a) and (b). Notice that the subscript does not correspond to the distance between two sites, and the hopping distance  $r$  is within the range  $r \leq \sqrt{3}L_M$ . In the present model, we have  $t_1 \approx 0.330$  meV,  $t_2 \approx \pm 0.0969i$  meV (pure imaginary),  $t_3 \approx 0$  meV,  $t_4 \approx 0.0347$  meV, and  $t_5 \approx 0.117$  meV.



With real  $t_1$  and imaginary  $t_2 = it'_2$  only, tight-binding model (7) becomes the primitive model proposed in Ref. 4,

$$H_0 = \sum_{\langle ij \rangle} t_1 \mathbf{c}_i^\dagger \cdot \mathbf{c}_j + \sum_{\langle ij \rangle'} t'_2 (\mathbf{c}_i^\dagger \times \mathbf{c}_j)_z + h.c. \quad (8)$$

where  $\mathbf{c}_i = (c_{i,x}, c_{i,y})^T$  with  $c_{i,x(y)}$  annihilating an electron with  $p_{x(y)}$ -orbital at site  $i$ , and  $c_{i\xi} = c_{ix} + i\xi c_{iy}$ . The primitive tight-binding model (8) gives rise to a spectrum with particle-hole symmetry and Dirac nodes at  $\bar{K}, \bar{K}'$  points. We then consider effects of adding more hopping terms into primitive model (8). First, a complex  $t_1$  will not change the spectrum as long as the magnitude keeps the same. This is because  $t_1$  denotes hopping between two sublattices and hence its phase can always be fixed by changing the relative phase between sublattices. Second, when  $\text{Re}(t_2) \neq 0$ , the particle-hole symmetry is found broken. Thus  $t_2$  should be pure imaginary to preserve particle-hole symmetry in the present model. Third, when  $\text{Re}(t_3) \neq 0$ , the particle-hole symmetry is found broken, and when  $\text{Im}(t_3) \neq 0$ , the spectrum at  $\bar{K}, \bar{K}'$  points is found gapped. As a result,  $t_3$  must vanish to preserve both particle-hole symmetry and Dirac nodes at  $\bar{K}, \bar{K}'$  points. At last, the nonzero  $t_4, t_5$  terms will modify the quantitative details of the primitive model (8) and preserves particle-hole symmetry and Dirac nodes at  $\bar{K}, \bar{K}'$  points, thus  $t_4, t_5$  are allowed. These terms change the shape of Fermi surfaces and hence the effective mass  $m_{\bar{\Gamma}}$  at  $\bar{\Gamma}$  point and the Fermi velocity  $v$  at  $\bar{K}, \bar{K}'$  points. In fact  $m_{\bar{\Gamma}}^{-1} = \frac{1}{2}t_1 + 2t_4 + 7t_5$  and  $v = \frac{\sqrt{3}}{2}(t_1 - 2t_4 - t_5)$  if  $t_1, t_4, t_5 \in \mathbb{R}$ .

Figure 5 presents the band structure in the effective tight-binding models with (a)  $t_1$  and  $t_2$ , (b)  $t_1, t_2$  and  $t_5$  and (c) all the hopping parameters within the distance  $r < 9L_M$ . Dashed line indicates the original energy band of the effective continuum model.

In realistic band structures from tight-binding and first-principle calculations, it is found that the particle-hole symmetry is broken while to a good approximation the Dirac nodes at  $\bar{K}, \bar{K}'$  points are preserved at small twist angles. Hence for realistic band structures we expect  $t_2$  can be complex and  $t_3$  can be nonzero. Furthermore, we can also break the orbital U(1) symmetry by introducing hopping terms such as the nearest-neighbor hopping term given in Ref. 4. Although the U(1) breaking hopping terms are tiny, they will affect the ultralow-energy structure near  $\bar{K}, \bar{K}'$  points. A detailed analysis of Dirac nodes and mass generation will be presented in a forthcoming work.

## VI. ELECTRON-ELECTRON INTERACTION

We can calculate the electron-electron interaction parameters between the Wannier orbitals directly from the wave functions obtained above. The direct Coulomb interaction  $V$  and the exchange interaction  $J$  between

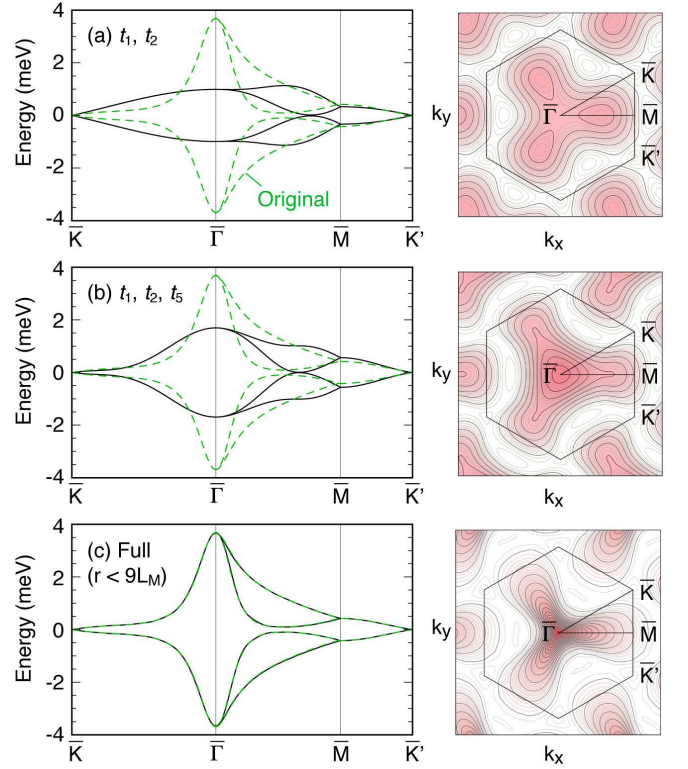


FIG. 5. Band structure in the effective tight-binding model for  $\theta = 1.05^\circ$ , with (a)  $t_1$  and  $t_2$ , (b)  $t_1, t_2$  and  $t_5$  and (c) all the hopping parameters within the distance  $r < 9L_M$ . Dashed line indicates the original energy band of the effective continuum model. Right panels show the corresponding contour plots of  $E_2(\mathbf{k})$  for the valley  $\xi = +$ .

$|\mathbf{R}, m\rangle$  and  $|\mathbf{R}', m'\rangle$  are defined by

$$V_{\mathbf{R}'m', \mathbf{R}m} = \sum_{XX'} \iint d\mathbf{r} d\mathbf{r}' |\psi_{\mathbf{R}'m'}^{X'}(\mathbf{r}')|^2 \frac{e^2}{\epsilon|\mathbf{r} - \mathbf{r}'|} |\psi_{\mathbf{R}m}^X(\mathbf{r})|^2, \quad (9)$$

$$J_{\mathbf{R}'m', \mathbf{R}m} = \sum_{XX'} \iint d\mathbf{r} d\mathbf{r}' \times \psi_{\mathbf{R}'m'}^{X'*}(\mathbf{r}') \psi_{\mathbf{R}m}^{X*}(\mathbf{r}) \frac{e^2}{\epsilon|\mathbf{r} - \mathbf{r}'|} \psi_{\mathbf{R}'m'}^X(\mathbf{r}) \psi_{\mathbf{R}m}^{X'}(\mathbf{r}'), \quad (10)$$

where  $\epsilon$  is the dielectric constant induced by the electrons in other bands and by the external environment (e.g., the substrate). The direct term is the classical Coulomb interaction and it works for any combinations of spin and valley. On the other hand, the exchange interaction works only for the same spin and the same valley. Rigorously speaking, the exchange term between different valleys (and the same spin) is not exactly zero, but there the integral of  $e^{i(\mathbf{K}_+ - \mathbf{K}_-) \cdot (\mathbf{r} - \mathbf{r}')}/|\mathbf{r} - \mathbf{r}'|$  in Eq. (10) becomes much smaller than that for the same valley, so we neglect it.

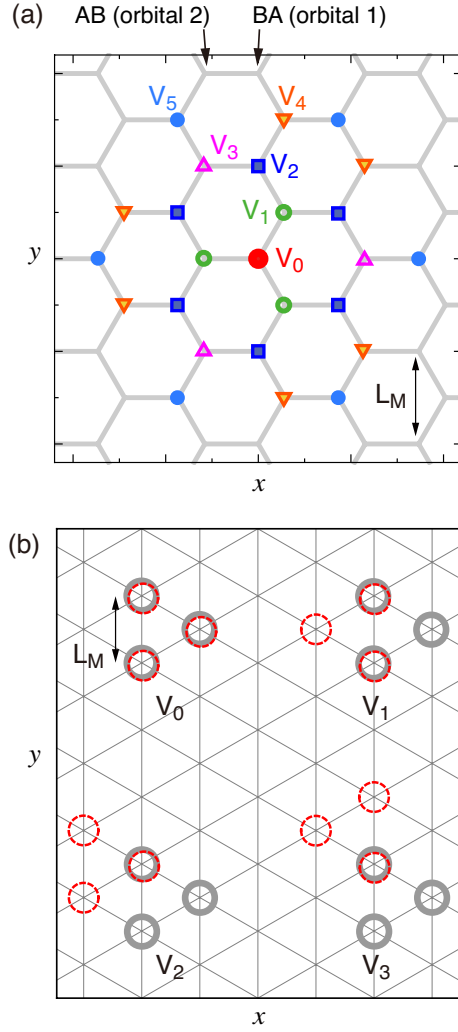


FIG. 6. (a) Labeling of the direct Coulomb interaction at different distances.  $V_0, V_1, V_2 \dots$  represent the potential amplitudes between the origin and the indicated lattice points. (b) Overlapping of two Wannier orbitals in the configuration  $V_0, V_1, V_2, V_3$ . The three circles of the same line type represent the three peaks of a single Wannier state [Fig. 3].

TABLE I. Direct interaction  $V_n$  and the exchange interaction  $J_n$  for the Wannier orbitals in units of  $e^2/(\epsilon L_M)$ . The definition of  $V_0, V_1 \dots$  is presented in Fig. 6(a).  $V_n^{(\text{approx})}$  is the direct interaction terms estimated by the point-charge approximation (see the text).

$n$	0	1	2	3	4	5
$V_n$	1.857	1.533	1.145	1.068	0.697	0.614
$V_n^{(\text{approx})}$	1.857	1.524	1.136	1.081	0.679	0.610
$J_n$	N/A	0.376	0.0645	0.010	0.014	0.001

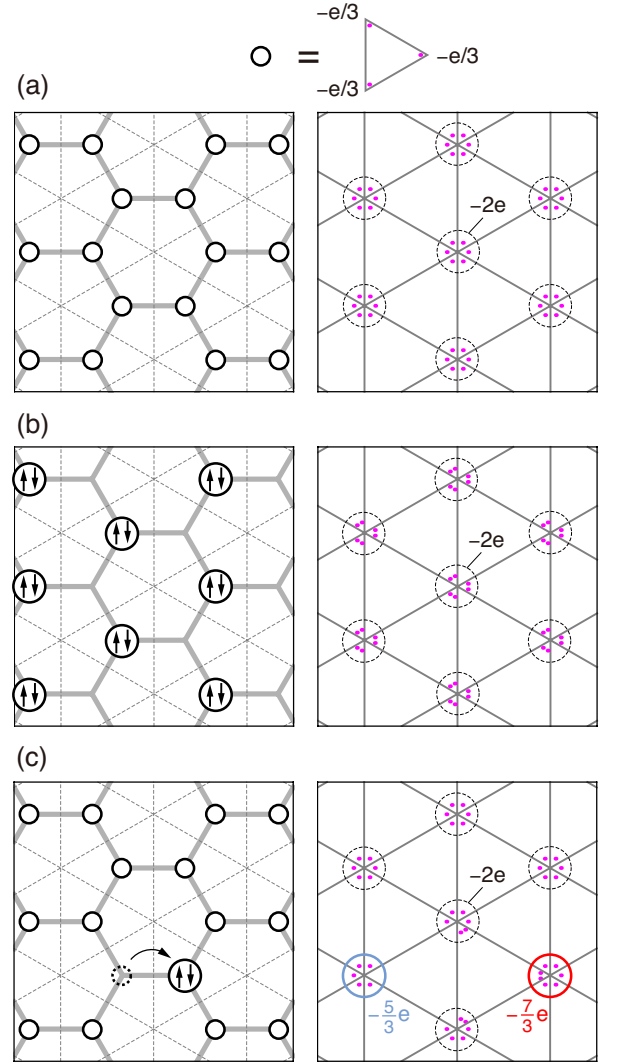


FIG. 7. Several conceivable many-body states illustrated in the honeycomb lattice picture (left) and the fractional charge picture (right). (a) The homogeneous state where an electron resides at every sublattice. (b) The charge-ordered state where two electrons enter every two sublattice. Opposite arrows in a single site represent two electrons with different spins or valley pseudospins. (c) An excited state from the state (a) where an electron is transferred from a single site to another.

We label the direct interaction terms at different distances as  $V_0, V_1, V_2 \dots$  as in Fig. 6(a), where  $V_0$  is the on-site interaction,  $V_1$  is the nearest neighbor interaction and so forth. Similarly the exchange terms can be labeled as  $J_1, J_2 \dots$ , where  $J_0$  does not exist due to the Pauli principle. The calculated interaction parameters are listed in Table I. Here we notice that the on-site interaction  $V_0$  is not much greater than others, but it is in a similar magnitude to the nearest-neighbor interaction  $V_1$ . The further interactions  $V_2$  and  $V_3$  are more than half of  $V_0$ . This is quite different from usual Hubbard-type



models where  $V_0$  dominates the interaction effect. The peculiar distance dependence of Coulomb interaction in this model is closely related to the three-peak structure of the Wannier orbital. For a single electron, each of three peaks accommodates the electric charge of  $-e/3$ , and thus the interacting potential between two electrons can be written as a summation over the nine combinations of those fractional charges. The direct Coulomb potential between two fractional charges located at the same peak (i.e., the "on-site interaction" for the fractional charges) is  $u_0 \approx (e/3)^2/\epsilon/(0.28L_M)$ , while the potential between different peaks is well approximated by that for the point charges, i.e.,  $(e/3)^2/\epsilon/r$ , where  $r$  is the distance between the peak centers. The direct interaction terms estimated by this approximation are presented as  $V_n^{(\text{approx})}$  in Table I, where the error is found to be 1% or less.

Obviously the dominant contribution to  $V_n$  comes from the on-site part  $u_0$ . As shown in Fig. 6(b), the electrons located at the same orbital ( $V_0$ ) share all the three peaks, the nearest neighbor configuration ( $V_1$ ) the two peaks, and the next nearest ones ( $V_2, V_3$ ) a single peak. Therefore, the on-site interaction of the fractional charges included in  $V_0, V_1, V_2, V_3$  is  $3u_0, 2u_0, u_0, u_0$ , respectively, and this explains the dominant part of the relative amplitudes of  $V_n$ 's.

At the filling of two electrons per super cell, in particular, the triangular charge distribution results in an unexpected degeneracy of two different many-body states shown in Fig. 7, with (a) a homogeneous state where an electron resides at every sublattice of the honeycomb lattice, and (b) a charge-ordered state where two electrons enter every two sublattice. It may seem that the direct Coulomb energy in (b) is greater than in (a) because of the double occupancy. However, since an electron at the honeycomb site is actually composed of three  $1/3$  charges at the triangle corners, the states (a) and (b) have nearly identical charge distribution as shown in the right panels, where the charge of  $-2e$  is registered to every AA points. Considering that the direct Coulomb interaction is very well approximated by the simple point-charge model as argued above, the total direct energies of (a) and (b) must be nearly equal. The competing nature of the two completely different states may suggest a nontrivial many-body ground state. For further consideration, we need to include the exchange interaction and also the kinetic energy. Lastly, Fig. 7(c) illustrates an excitation from the state (a), where an electron is transferred from a single honeycomb site to another. This actually corresponds to a pair creation of the fractional charges ( $\pm 1/3$ ) $e$  as shown in the right panel. This is another intriguing property at this filling factor.

## VII. CONCLUSION

An extended Hubbard model is obtained for the nearly flat band in the low-angle TBG by starting from the Bloch states in a realistic continuum model. The ob-

tained Wannier localized state is centered at AB or BA point to form a honeycomb lattice. The wave function of the Wannier orbital takes a triangular form which peaks at three AA spots surrounding the center, and it leads to a competition between the on-site interaction and the neighboring interaction. At the filling of two electrons per super cell, in particular, we have an unusual degeneracy of the a charge-ordered state and a homogeneous state, which implies a nontrivial nature of the ground state. The detailed studies for the many-body ground states in this model will be left for future works.

## VIII. ACKNOWLEDGMENT

MK thanks the fruitful discussions with Pilkung Moon and Nguyen N. T. Nam. MK acknowledges the financial support of JSPS KAKENHI Grant Number JP17K05496. NFQY and LF are supported by the DOE Office of Basic Energy Sciences, Division of Materials Sciences and Engineering under award de-sc0010526. LF is partly supported by the David and Lucile Packard Foundation. TK is supported by JSPS KAKENHI Grant Number JP18K03442 and JST PRESTO Grant Number JPMJPR15N5. KK is supported by JSPS KAKENHI Grant Number JP18H01860.

*Note added:* After completion of the present study, we have come to notice that a recent preprint which also reports the maximally-localized Wannier states for TBG.<sup>45</sup>

## Appendix A: Derivation of the effective continuum model under corrugation

We derive the effective interlayer interaction of a corrugated TBG in Eq. (2) following the method in Ref. 34. We start from the single-orbital tight-binding model for  $p_z$  orbital of carbon atoms. We assume that the transfer integral between any two orbitals is written in terms of the Slater-Koster form as,

$$-t(\mathbf{R}) = V_{pp\pi} \left[ 1 - \left( \frac{\mathbf{R} \cdot \mathbf{e}_z}{R} \right)^2 \right] + V_{pp\sigma} \left( \frac{\mathbf{R} \cdot \mathbf{e}_z}{R} \right)^2, \\ V_{pp\pi} = V_{pp\pi}^0 e^{-(R-a_0)/r_0}, \quad V_{pp\sigma} = V_{pp\sigma}^0 e^{-(R-d_0)/r_0}. \quad (\text{A1})$$

Here  $\mathbf{e}_z$  is the unit vector perpendicular to the graphene plane,  $a_0 = a/\sqrt{3} \approx 0.142$  nm is the distance of neighboring  $A$  and  $B$  sites on graphene, and  $d_0 \approx 0.335$  nm is the interlayer spacing of graphite. The parameter  $V_{pp\pi}^0$  is the transfer integral between the nearest-neighbor atoms on graphene, and  $V_{pp\sigma}^0$  is the transfer integral between vertically located atoms on the neighboring layers of graphite. We take  $V_{pp\pi}^0 \approx -2.7$  eV,  $V_{pp\sigma}^0 \approx 0.48$  eV, to fit the dispersions of monolayer graphene.<sup>34</sup> Here  $r_0$  is the decay length of the transfer integral, and is chosen as  $0.184a$  so that the next nearest intralayer coupling becomes  $0.1V_{pp\pi}^0$ .

To construct the Hamiltonian matrix, we define the Bloch wave bases as

$$\begin{aligned} |\mathbf{k}, A_l\rangle &= \frac{1}{\sqrt{N}} \sum_{\mathbf{R}_{A_l}} e^{i\mathbf{k} \cdot \mathbf{R}_{A_l}} |\mathbf{R}_{A_l}\rangle, \\ |\mathbf{k}, B_l\rangle &= \frac{1}{\sqrt{N}} \sum_{\mathbf{R}_{B_l}} e^{i\mathbf{k} \cdot \mathbf{R}_{B_l}} |\mathbf{R}_{B_l}\rangle, \end{aligned} \quad (\text{A2})$$

where the position  $\mathbf{R}_{A_l}(\mathbf{R}_{B_l})$  runs over all  $A(B)$  sites on the layer  $l(=1, 2)$ ,  $N$  is the number of monolayer's unit cell in the whole system, and  $\mathbf{k}$  is two-dimensional Bloch wave vector defined in the first Brillouin zone of monolayer on the layer  $l$ .

For the interlayer coupling, we first consider a non-rotated bilayer graphene with  $\theta = 0$  and a constant in-plane displacement  $\boldsymbol{\delta}$  from AA stacking. The unit cell is spanned by monolayer's lattice vectors,  $\mathbf{a}_1 = a(1, 0)$  and  $\mathbf{a}_2 = a(1/2, \sqrt{3}/2)$ , which are now shared by both layers. Then the lattice points of the sublattice  $X(=A_1, B_1, A_2, B_2)$  are given by

$$\begin{aligned} \mathbf{R}_{A_1} &= n_1 \mathbf{a}_1 + n_2 \mathbf{a}_2 + \boldsymbol{\tau}_{A_1}, \\ \mathbf{R}_{B_1} &= n_1 \mathbf{a}_1 + n_2 \mathbf{a}_2 + \boldsymbol{\tau}_{B_1}, \\ \mathbf{R}_{A_2} &= n_1 \mathbf{a}_1 + n_2 \mathbf{a}_2 + \boldsymbol{\tau}_{A_2} + \boldsymbol{\delta} + d(\boldsymbol{\delta}) \mathbf{e}_z, \\ \mathbf{R}_{B_2} &= n_1 \mathbf{a}_1 + n_2 \mathbf{a}_2 + \boldsymbol{\tau}_{B_2} + \boldsymbol{\delta} + d(\boldsymbol{\delta}) \mathbf{e}_z. \end{aligned} \quad (\text{A3})$$

Here  $\boldsymbol{\tau}_{A_1} = \boldsymbol{\tau}_{A_2} = 0$ ,  $\boldsymbol{\tau}_{B_1} = \boldsymbol{\tau}_{B_2} = -\boldsymbol{\tau}_1$  with  $\boldsymbol{\tau}_1 = (2\mathbf{a}_2 - \mathbf{a}_1)/3 = (0, a/\sqrt{3})$ , and  $d(\boldsymbol{\delta})$  is the optimized interlayer distance which generally depends on  $\boldsymbol{\delta}$ . Note that  $d(\boldsymbol{\delta})$  is a periodic function of  $\boldsymbol{\delta}$  with periods of  $\mathbf{a}_1$  and  $\mathbf{a}_2$ , because the interlayer shift by a lattice vector just gives the equivalent structure. It is known that the interlayer spacing takes the maximum value  $d_{AA}$  at AA stacking ( $\boldsymbol{\delta} = 0$ ), and the minimum at  $d_{AB}$  at AB stacking ( $\boldsymbol{\delta} = \boldsymbol{\tau}_1$ )<sup>46</sup>. Here we adopt  $d_{AA} = 0.360$  nm and  $d_{AB} = 0.335$  nm.<sup>40,46</sup> The distance at intermediate  $\boldsymbol{\delta}$  can be interpolated by

$$d(\boldsymbol{\delta}) = d_0 + 2d_1 \sum_{j=1}^3 \cos \mathbf{a}_j^* \boldsymbol{\delta}, \quad (\text{A4})$$

with

$$d_0 = \frac{1}{3}(d_{AA} + 2d_{AB}), \quad (\text{A5})$$

$$d_1 = \frac{1}{9}(d_{AA} - d_{AB}). \quad (\text{A6})$$

The interlayer matrix element between from  $X = A_1, B_1$  to  $X' = A_2, B_2$  is obtained by taking all the transfer integrals between atoms of layer 1 and layer 2. It is

explicitly written as

$$\begin{aligned} U_{X'X}(\mathbf{k}, \boldsymbol{\delta}) &\equiv \langle \mathbf{k}, X' | H | \mathbf{k}, X \rangle \\ &= \sum_{n_1, n_2} -t[n_1 \mathbf{a}_1 + n_2 \mathbf{a}_2 + \boldsymbol{\tau}_{X'X} + \boldsymbol{\delta} + d(\boldsymbol{\delta}) \mathbf{e}_z] \\ &\quad \times \exp[-i\mathbf{k} \cdot (n_1 \mathbf{a}_1 + n_2 \mathbf{a}_2 + \boldsymbol{\tau}_{X'X} + \boldsymbol{\delta})], \end{aligned} \quad (\text{A7})$$

where  $\boldsymbol{\tau}_{X'X} = \boldsymbol{\tau}_{X'} - \boldsymbol{\tau}_X$ .  $U_{X'X}(\mathbf{k}, \boldsymbol{\delta})$  is also a periodic function of  $\boldsymbol{\delta}$  with periods  $\mathbf{a}_1$  and  $\mathbf{a}_2$ , and therefore it can be written as a Fourier expansion,

$$\begin{aligned} U_{X'X}(\mathbf{k}, \boldsymbol{\delta}) &\equiv \langle \mathbf{k}, X' | H | \mathbf{k}, X \rangle \\ &= \sum_{m_1, m_2} \tilde{U}_{X'X}(m_1 \mathbf{a}_1^* + m_2 \mathbf{a}_2^* + \mathbf{k}) \\ &\quad \times \exp[i(m_1 \mathbf{a}_1^* + m_2 \mathbf{a}_2^*) \cdot (\boldsymbol{\delta} + \boldsymbol{\tau}_{X'X})]. \end{aligned} \quad (\text{A8})$$

Here we defined

$$\tilde{U}_{X'X}(\mathbf{q}) = -\frac{1}{S_0} \int t[\mathbf{R} + d(\mathbf{R} - \boldsymbol{\tau}_{X'X}) \mathbf{e}_z] e^{-i\mathbf{q} \cdot \mathbf{R}} d^2 \mathbf{R}, \quad (\text{A9})$$

where  $S_0 = (\sqrt{3}/2)a^2$  is the unit area of monolayer graphene, and the integral in  $\mathbf{R}$  is over the infinite two-dimensional space.  $\tilde{U}_{X'X}(\mathbf{q})$  is circular symmetric and only depends on  $|\mathbf{q}|$ . Since  $t(\mathbf{R})$  exponentially decays in  $R \sim r_0$ , the Fourier transform  $\tilde{U}_{X'X}(\mathbf{q})$  decays in  $q \sim 1/r_0$ .

When we rotate one graphene layer to another by a small twist angle  $\theta$ , the local lattice structure in the moiré pattern is approximately viewed as a non-rotated bilayer graphene, where the displacement  $\boldsymbol{\delta}$  slowly depends on the position  $\mathbf{r}$  in accordance with<sup>38</sup>

$$\boldsymbol{\delta}(\mathbf{r}) = [R(\theta/2) - R(-\theta/2)]\mathbf{r}. \quad (\text{A10})$$

The interlayer matrix element for valley  $\xi$  is then approximately written by  $U_{X'X}[\mathbf{K}_\xi, \boldsymbol{\delta}(\mathbf{r})]$ .<sup>34</sup> Using Eqs. (A8) and (A10), we obtain

$$\begin{aligned} U_{X'X}[\mathbf{K}_\xi, \boldsymbol{\delta}(\mathbf{r})] &= \sum_{m_1, m_2} \tilde{U}_{X'X}(m_1 \mathbf{a}_1^* + m_2 \mathbf{a}_2^* + \mathbf{K}_\xi) \\ &\quad \times \exp[i(m_1 \mathbf{a}_1^* + m_2 \mathbf{a}_2^*) \cdot \boldsymbol{\tau}_{X'X}] \\ &\quad \times \exp[i(m_1 \mathbf{G}_1^M + m_2 \mathbf{G}_2^M) \cdot \mathbf{r}], \end{aligned} \quad (\text{A11})$$

where we used the relationship  $\mathbf{a}_i^* \cdot \boldsymbol{\delta}(\mathbf{r}) = \mathbf{G}_i^M \cdot \mathbf{r}$ . Now we see that Eq. (A11) is periodic in  $\mathbf{r}$  with the moiré reciprocal vectors  $\mathbf{G}_i^M$ . Since  $\tilde{U}_{X'X}(\mathbf{q})$  rapidly decays in  $q$ , we only need a few Fourier components in Eq. (A11). By taking the largest three terms given by  $(m_1, m_2) = (0, 0), \xi(1, 0), \xi(1, 1)$ , we have the Hamiltonian in Eq. (2), where

$$\begin{aligned} u &= -\frac{1}{S_0} \int t[\mathbf{R} + d(\mathbf{R}) \mathbf{e}_z] e^{-i\mathbf{K}_\xi \cdot \mathbf{R}} d^2 \mathbf{R}, \\ u' &= -\frac{1}{S_0} \int t[\mathbf{R} + d(\mathbf{R} - \boldsymbol{\tau}_1) \mathbf{e}_z] e^{-i\mathbf{K}_\xi \cdot \mathbf{R}} d^2 \mathbf{R}. \end{aligned} \quad (\text{A12})$$

We obtain  $u = 0.0797\text{eV}$  and  $u' = 0.0975\text{eV}$  for the present parameters. In a flat TBG, the interlayer distance  $d(\boldsymbol{\delta})$  is constant and therefore we have  $u = u'$ .<sup>34</sup>

- 
- \* koshino@phys.sci.osaka-u.ac.jp
- <sup>1</sup> Y. Cao, V. Fatemi, S. Fang, K. Watanabe, T. Taniguchi, E. Kaxiras, and P. Jarillo-Herrero, *Nature* **556**, 43 (2018).
  - <sup>2</sup> Y. Cao, V. Fatemi, A. Demir, S. Fang, S. L. Tomarken, J. Y. Luo, J. D. Sanchez-Yamagishi, K. Watanabe, T. Taniguchi, E. Kaxiras, R. C. Ashoori, and P. Jarillo-Herrero, *Nature* **556**, 80 (2018).
  - <sup>3</sup> C. Xu and L. Balents, arXiv preprint arXiv:1803.08057 (2018).
  - <sup>4</sup> N. F. Yuan and L. Fu, arXiv preprint arXiv:1803.09699 (2018).
  - <sup>5</sup> H. C. Po, L. Zou, A. Vishwanath, and T. Senthil, arXiv preprint arXiv:1803.09742 (2018).
  - <sup>6</sup> B. Roy and V. Juricic, arXiv preprint arXiv:1803.11190 (2018).
  - <sup>7</sup> H. Guo, X. Zhu, S. Feng, and R. T. Scalettar, arXiv preprint arXiv:1804.00159 (2018).
  - <sup>8</sup> B. Padhi, C. Setty, and P. W. Phillips, arXiv preprint arXiv:1804.01101 (2018).
  - <sup>9</sup> J. F. Dodaro, S. A. Kivelson, Y. Schattner, X.-Q. Sun, and C. Wang, arXiv preprint arXiv:1804.03162 (2018).
  - <sup>10</sup> T. Huang, L. Zhang, and T. Ma, arXiv preprint arXiv:1804.06096 (2018).
  - <sup>11</sup> L. Zhang, arXiv preprint arXiv:1804.09047 (2018).
  - <sup>12</sup> S. Ray and T. Das, arXiv preprint arXiv:1804.09674 (2018).
  - <sup>13</sup> C.-C. Liu, L.-D. Zhang, W.-Q. Chen, and F. Yang, arXiv preprint arXiv:1804.10009 (2018).
  - <sup>14</sup> X. Y. Xu, K. Law, and P. A. Lee, arXiv preprint arXiv:1805.00478 (2018).
  - <sup>15</sup> T. J. Peltonen, R. Ojaärvi, and T. T. Heikkilä, arXiv preprint arXiv:1805.01039 (2018).
  - <sup>16</sup> M. Fidrysiak, M. Zegrodnik, and J. Spalek, arXiv preprint arXiv:1805.01179 (2018).
  - <sup>17</sup> C. Berger, Z. Song, X. Li, X. Wu, N. Brown, C. Naud, D. Mayou, T. Li, J. Hass, A. N. Marchenkov, E. H. Conrad, P. N. First, and W. A. de Heer, *Science* **312**, 1191 (2006).
  - <sup>18</sup> J. Hass, R. Feng, J. Millan-Otoya, X. Li, M. Sprinkle, P. First, W. De Heer, E. Conrad, and C. Berger, *Phys. Rev. B* **75**, 214109 (2007).
  - <sup>19</sup> J. Hass, F. Varchon, J. Millan-Otoya, M. Sprinkle, N. Sharma, W. de Heer, C. Berger, P. First, L. Magaud, and E. Conrad, *Phys. Rev. Lett.* **100**, 125504 (2008).
  - <sup>20</sup> G. Li, A. Luican, J. M. B. Lopes dos Santos, A. Neto, A. Reina, J. Kong, and E. Andrei, *Nature Physics* **6**, 109 (2009).
  - <sup>21</sup> D. Miller, K. Kubista, G. Rutter, M. Ruan, W. de Heer, P. First, and J. Stroscio, *Phys. Rev. B* **81**, 125427 (2010).
  - <sup>22</sup> A. Luican, G. Li, A. Reina, J. Kong, R. Nair, K. Novoselov, A. Geim, and E. Andrei, *Phys. Rev. Lett.* **106**, 126802 (2011).
  - <sup>23</sup> J. Lopes dos Santos, N. Peres, and A. Castro Neto, *Phys. Rev. Lett.* **99**, 256802 (2007).
  - <sup>24</sup> E. Mele, *Phys. Rev. B* **81**, 161405 (2010).
  - <sup>25</sup> G. Trambly de Laissardière, D. Mayou, and L. Magaud, *Nano Lett.* **10**, 804 (2010).
  - <sup>26</sup> S. Shallcross, S. Sharma, E. Kandelaki, and O. Pankratov, *Phys. Rev. B* **81**, 165105 (2010).
  - <sup>27</sup> E. Morell, J. Correa, P. Vargas, M. Pacheco, and Z. Barticevic, *Phys. Rev. B* **82**, 121407 (2010).
  - <sup>28</sup> R. Bistritzer and A. MacDonald, *Proc. Natl. Acad. Sci.* **108**, 12233 (2011).
  - <sup>29</sup> M. Kindermann and P. First, *Phys. Rev. B* **83**, 045425 (2011).
  - <sup>30</sup> L. Xian, S. Barraza-Lopez, and M. Chou, *Phys. Rev. B* **84**, 075425 (2011).
  - <sup>31</sup> J. M. B. Lopes dos Santos, N. M. R. Peres, and A. H. Castro Neto, *Phys. Rev. B* **86**, 155449 (2012).
  - <sup>32</sup> P. Moon and M. Koshino, *Phys. Rev. B* **85**, 195458 (2012).
  - <sup>33</sup> G. T. de Laissardière, D. Mayou, and L. Magaud, *Phys. Rev. B* **86**, 125413 (2012).
  - <sup>34</sup> P. Moon and M. Koshino, *Phys. Rev. B* **87**, 205404 (2013).
  - <sup>35</sup> M. Koshino, *New J. Phys.* **17**, 015014 (2015).
  - <sup>36</sup> M. Koshino and P. Moon, *J. Phys. Soc. Jpn.* **84**, 121001 (2015).
  - <sup>37</sup> Y. Cao, J. Luo, V. Fatemi, S. Fang, J. Sanchez-Yamagishi, K. Watanabe, T. Taniguchi, E. Kaxiras, and P. Jarillo-Herrero, *Physical Review Letters* **117**, 116804 (2016).
  - <sup>38</sup> N. N. T. Nam and M. Koshino, *Phys. Rev. B* **96**, 075311 (2017).
  - <sup>39</sup> N. Marzari and D. Vanderbilt, *Phys. Rev. B* **56**, 12847 (1997).
  - <sup>40</sup> K. Uchida, S. Furuya, J.-I. Iwata, and A. Oshiyama, *Phys. Rev. B* **90**, 155451 (2014).
  - <sup>41</sup> M. van Wijk, A. Schuring, M. Katsnelson, and A. Fasolino, *2D Mater.* **2**, 034010 (2015).
  - <sup>42</sup> S. Dai, Y. Xiang, and D. J. Srolovitz, *Nano letters* **16**, 5923 (2016).
  - <sup>43</sup> S. K. Jain, V. Juričić, and G. T. Barkema, *2D Mater.* **4**, 015018 (2016).
  - <sup>44</sup> In the data file, each line contains the components of the vector  $\mathbf{R}$  in terms of the lattice vectors  $\mathbf{L}_i^M (i = 1, 2)$ , the orbital indices  $m$  and  $n$ , and the real and imaginary parts of the Hamiltonian matrix element  $\langle \mathbf{R}, m | H | \mathbf{0}, n \rangle$ . Here the lattice vectors are taken as  $\mathbf{L}_1^M = (\sqrt{3}/2, 1/2)L_M$ ,  $\mathbf{L}_2^M = (0, 1)L_M$ , and the sublattice positions of orbital 1 and 2 in the same unit cell are defined by  $\mathbf{r}_{BA} = (1/2, \sqrt{3}/2)(L_M/\sqrt{3})$  and  $\mathbf{r}_{AB} = (-1/2, \sqrt{3}/2)(L_M/\sqrt{3})$ , respectively. We omit the hopping parameters of distance greater than  $9L_M$ .
  - <sup>45</sup> J. Kang and O. Vafek, arXiv preprint arXiv:1805.04918 (2018).
  - <sup>46</sup> J.-K. Lee, S.-C. Lee, J.-P. Ahn, S.-C. Kim, J. I. Wilson, and P. John, *The Journal of chemical physics* **129**, 234709 (2008).